Identification of Bare-Airframe Dynamics from Closed-Loop Data Using Multisine Inputs and Frequency Responses

Jared A. Grauer*
NASA Langley Research Center, Hampton, Virginia, 23681

Matthew J. Boucher†
NASA Armstrong Flight Research Center, Edwards, California, 93523

A method is presented for computing multiple-input multiple-output frequency responses of bare-airframe dynamics for systems excited using orthogonal phase-optimized multisines and including correlated data arising from control mixing or feedback control. The estimation was posed as the solution to an underdetermined system of linear equations, for which additional information was supplied using interpolation of the frequency responses. A simulation model of the NASA T-2 aircraft having two inputs and two outputs was used to investigate the method in the open-loop configuration and under closed-loop control. The method was also applied to flight test data from the X-56A aeroelastic demonstrator having five inputs and ten outputs and flying under closed-loop control with additional control allocation mixing. Results demonstrated that the proposed method accurately estimates the bare airframe frequency responses in the presence of correlated data from control mixing and feedback control. Results also agreed with estimates obtained using different methods that are less sensitive to correlated inputs.

I. Nomenclature

a_z	=	vertical accelerometer measurement, g
$\bar{c}$	=	mean aerodynamic chord, ft
f	=	frequency, Hz
g	=	gravitational acceleration, ft/s^2
h	=	altitude, ft
I_{yy}	=	pitch moment of inertia, slug-ft^2
j	=	imaginary number, = $\sqrt{-1}$
m	=	aircraft mass, slug
q	=	pitch rate, rad/s
$\bar{q}$	=	dynamic pressure, lbf/ft^2
S	=	wing reference area, ft^2
t	=	time, s
V	=	airspeed, ft/s
Z, M	=	vertical force and pitching moment
α	=	angle of attack, rad
Δ	=	perturbation
δ	=	control surface deflection, rad
ζ	=	damping ratio
λ	=	pole location
ω_n	=	natural frequency, rad/s

*Research Engineer, Dynamic Systems and Control Branch, MS 308, Associate Fellow AIAA.
†Research Engineer, Controls and Dynamics Branch, MS 4840D, Member AIAA.

II. Introduction

Flight test data for research aircraft often contain correlated inputs, for example arising from input control mixing or feedback control. These correlations obscure the effect of inputs on the output responses, inhibiting system identification of the bare-airframe dynamics [1]. One approach to this problem is to change the experiment design by adding unique perturbation excitations to each control surface command after the flight control system but before the actuator rate and position limiting. These excitations can lower pairwise correlations of the inputs so that standard estimation methods can be applied in the usual manner. This approach began with the open-loop unstable X-29 aircraft [2] and has been successfully used in flight tests with the F-18 HARV, X-31, F-15B ACTIVE, X-43A, NASA T-2, and many others.

When frequency responses are used for the identification of bare-airframe dynamics from correlated data, additional considerations are necessary, such as those discussed in Ref. [3] using spectral methods. For moderately correlated inputs, contributions from secondary inputs can be used to condition modeling data or ignored. For highly-correlated inputs, the joint input-output method has been used [4, 5] to identify bare-airframe frequency responses by considering the bare-airframe inputs and outputs together as outputs from another reference input.

Another method for frequency response estimation was introduced in Refs. [1, 6]. Orthogonal phase-optimized multisine inputs were used to excite the aircraft by moving multiple control effectors at the same time but with different harmonic frequencies. Frequency responses were then computed by dividing Fourier transforms of measured input and output data at the harmonic frequencies. The method can be run in real-time for multiple-input multiple output (MIMO) systems and has been used to estimate dynamic models and stability margins, to detect sensor and actuator faults, and to expedite envelope expansion flight tests. However, as noted in Ref. [5], the accuracy of these frequency response estimates diminishes when data are correlated and contributions from secondary inputs are ignored. These errors are introduced because the harmonic frequencies are no longer unique to a particular input, which again obscures the effect of inputs on the output responses.

In this paper, the frequency response method in Refs. [1, 6] is extended to account for correlated secondary inputs, such as from control allocation or feedback control. The frequency response estimation is cast as a system of linear equations. Secondary inputs arising from mixing or feedback create additional unknown frequency response evaluations that render the system underdetermined. However, additional information can be supplied using interpolation, and the fully-determined system of linear equations can be efficiently solved for the unknown frequency responses using standard numerical routines. The solutions in Refs. [1, 6] are recovered in the limit as the input correlations decrease.

This paper is organized as follows. Section III summarizes the orthogonal phase-optimized multisine inputs and Fourier transform methods used to excite the system and transform the data into the frequency domain at harmonic frequencies. In Section IV, two sources of data are introduced. The first is a linear simulation model of the short period dynamics for the NASA T-2 subscale airplane. The second is the X-56A subscale aeroelastic demonstrator aircraft. Results using the T-2 simulation are presented in Section V for the open-loop configuration, and for when single and multiple control loops are closed by a feedback control law. These examples illustrate the performance of the method, demonstrate the effects of secondary inputs and how to account for them, and develop a general approach. Results presented in Section VI using X-56A flight test data demonstrate the method for a maneuver with control mixing and feedback control. Conclusions are drawn in Section VII.

Due to ITAR restrictions associated with the X-56A airplane, numerical values for that data are not given in this paper. The experiment design and system identification analysis in Sections V and VI used routines contained in the MATLAB®-based software package called System IDentification Programs for AirCraft, or SIDPAC [7].

III. Methods

A. Orthogonal Phase-Optimized Multisine Inputs

The orthogonal phase-optimized multisine inputs, hereafter referred to as multisines, were presented in Refs. [8, 9]. This section summarizes the design of those inputs and discusses implications and advantages for frequency response estimation. For more discussion on multisines or additional flight test examples, see Ref. [1] and the references therein.

Multisine inputs are applied over the time duration T, which defines the fundamental frequency $1/T$. Harmonic frequencies k/T are included in the multisines, where k is the integer harmonic number. When intended for frequency response estimation, T is a compromise between meeting operational requirements and achieving fine frequency resolution. The set of included harmonics, K, is chosen so the excitation spans the bandwidth of interest. Good modeling results usually necessitate at least two cycles of each frequency, making $2/T$ a practical lower limit. If lower frequencies

are desired, the excitation duration should be extended. For designing multisines for multiple inputs, K is divided into the subsets $K_1, K_2, \ldots, K_{n_u}$. Harmonics are typically assigned to these subsets in an alternating manner where each input has wide coverage over the excitation bandwidth.

Once the harmonics have been assigned to the inputs, each multisine is assembled as the sum of sinusoids

$$u_j(t) = \sum_{k \in K_j} a_k \sin\left(\frac{2\pi k}{T} t + \phi_k\right), \qquad \text{for } j = 1, 2, \ldots, n_u \tag{1}$$

The amplitudes a_k are designed according to desired power spectra for each input. A uniform distribution is often used, where

$$a_k = \frac{A_j}{\sqrt{M_j}}, \qquad \forall\, k \in K_j \tag{2}$$

and where M_j is the number of harmonics in K_j. In this case, each input has a single amplitude A_j selected to achieve adequate response amplitudes and signal-to-noise ratios. The amplitudes could instead be tailored for specific applications, such as attenuating known structural resonances or reducing excessive airspeed variation from phugoid excitation. The phase angles ϕ_k are optimized for each input to minimize the relative peak factor

$$RPF(u_j) = \frac{\max(u_j) - \min(u_j)}{2\sqrt{2}\ \mathrm{rms}(u_j)} \tag{3}$$

This optimization helps to keep the aircraft on condition, which is important for accurate linear modeling.

Multisine inputs are have many characteristics that are advantageous for frequency response estimation. One benefit is that because they are summations of harmonic sinusoids, multisines are mutually orthogonal and therefore can be applied to multiple inputs simultaneously for system identification. This property is in contrast to traditional types of inputs, which must be applied sequentially, one at a time, and therefore use more flight time. Another benefit is that multisine inputs produce steady-state response data (after initial transients decay), which is the information needed to estimate frequency responses. For linear systems, multisines are analogous to the original sine-dwell inputs used in early experiments for frequency response identification [10], but can include many frequencies on many inputs instead of a single frequency on a single input. Lastly, note that multisines can be designed using no more prior knowledge about the system in question than is needed for other identification inputs such as frequency sweeps or multi-steps.

B. Fourier Transforms

To estimate frequency responses, measured data are transformed from the time domain to the frequency domain. The analytical tool for doing this is the finite Fourier transform

$$x(\omega) = \int_0^T x(t)\, e^{-j\omega t}\, dt \tag{4}$$

where $x(t)$ and $x(\omega)$ are Fourier transform pairs and where $\omega = 2\pi f$ is the radian frequency. Equation (4) projects the measured data onto complex exponentials, alternatively represented as phased sinusoids.

Equation (4) can be evaluated in several ways. Fast Fourier transform (FFT) routines are not usually applied for modeling aircraft dynamics because they give relatively coarse frequency resolution over the bandwidths of interest. When the entire data record is available, as in batch post-flight analysis, a high-accuracy finite Fourier transform based on the chirp z-transform and cubic interpolation of the measured data can be used [1, 11]. Alternatively, when the sampling rate is much higher than the bandwidth of interest, a simpler Euler approximation

$$x(\omega) \simeq \Delta t \sum_{i=1}^{N} x(t_i)\, e^{-j\omega t_i} \tag{5}$$

can be used to approximate Eq. (4). This form can be made recursive for real-time analyses as

$$x_i(\omega) = \lambda\, x_{i-1}(\omega) + x(t_i)\, e^{-j\omega t_i} \tag{6}$$

where transforms are updated for each new sample with an addition and a multiplication. This simplicity facilitates the use with many measurements and frequencies using limited computational resources. The term λ is an exponential forgetting factor that can be adjusted to systematically discard past data and adapt to more recent information. For more detailed discussion on these techniques, see Refs. [1, 11, 12] and references therein.

IV. Test Aircraft

A. T-2 Short Period Simulation Model

The NASA T-2 subscale airplane, shown in Fig. 1, is a dynamically-scaled 5.5% version of a generic commercial transport aircraft. It has twin jet engines mounted under the wings and retractable tricycle landing gear. The aircraft is instrumented for modeling and control research and includes air data probes attached to booms mounted on each wing tip, two inertial measurement units, ambient air sensors, potentiometers on each of the 16 independent control surfaces, and other sensors.

Fig. 1 T-2 airplane (credit: NASA Langley Research Center).

The linearized short period model approximation of the T-2 bare-airframe dynamics used in Section V was

$$\begin{bmatrix} \dot{\alpha} \\ \dot{q} \end{bmatrix} = \begin{bmatrix} Z_\alpha & 1 + Z_q \\ M_\alpha & M_q \end{bmatrix} \begin{bmatrix} \alpha \\ q \end{bmatrix} + \begin{bmatrix} Z_{\delta_{eo}} & Z_{\delta_{ei}} \\ M_{\delta_{eo}} & M_{\delta_{ei}} \end{bmatrix} \begin{bmatrix} \delta_{eo} \\ \delta_{ei} \end{bmatrix} \tag{7a}$$

$$\begin{bmatrix} q \\ a_z \end{bmatrix} = \begin{bmatrix} 0 & 1 \\ \frac{V}{g} Z_\alpha & \frac{V}{g} Z_q \end{bmatrix} \begin{bmatrix} \alpha \\ q \end{bmatrix} + \begin{bmatrix} 0 & 0 \\ \frac{V}{g} Z_{\delta_{eo}} & \frac{V}{g} Z_{\delta_{ei}} \end{bmatrix} \begin{bmatrix} \delta_{eo} \\ \delta_{ei} \end{bmatrix} \tag{7b}$$

which has two inputs, two states, and two outputs. The horizontal tail on the T-2 includes four independent control surfaces. The inputs for Eq. (7) are the symmetric outboard and symmetric inboard elevator deflections

$$\delta_{eo} = \frac{1}{2} (\delta_{eol} + \delta_{eor}) \tag{8a}$$

$$\delta_{ei} = \frac{1}{2} (\delta_{eil} + \delta_{eir}) \tag{8b}$$

where the subscripts "o" and "i" denote outboard and inboard, and where "l" and "r" denote the left and right. The model state variables are the angle of attack at the aircraft center of mass and the pitch rate. The outputs are the pitch rate and vertical acceleration at the center of mass, as measured by a rate gyroscope and accelerometer, respectively. Parameters describing the flight condition, mass properties, and geometry properties of the airplane are listed in Table 1. The dimensional stability and control derivatives used in Eq. (7) are defined in terms of the corresponding nondimensional versions listed in Table 2 as

$$Z_\alpha = \frac{\bar{q}S}{mV} C_{Z_\alpha} \qquad Z_q = \frac{\bar{q}S\bar{c}}{2mV^2} C_{Z_q} \qquad Z_\delta = \frac{\bar{q}S}{mV} C_{Z_\delta} \tag{9a}$$

$$M_\alpha = \frac{\bar{q}S\bar{c}}{I_{yy}} C_{m_\alpha} \qquad M_q = \frac{\bar{q}S\bar{c}^2}{2VI_{yy}} C_{m_q} \qquad M_\delta = \frac{\bar{q}S\bar{c}}{I_{yy}} C_{m_\delta} \tag{9b}$$

These nondimensional stability and control derivatives were identified from flight test data using equation error in the frequency domain [1] and six repeated maneuvers where multisines were used on each of the 16 control surfaces [13].

The bare-airframe model was augmented with first-order actuator models

$$\frac{\delta(\omega)}{\delta_c(\omega)} = \frac{32.42}{j\omega + 32.42} \tag{10}$$

Table 1 T-2 simulation flight condition, mass properties, and geometry values.

Parameter	Value	Unit
V	130	ft/s
α	4.0	deg
δ_{eo}	−1.29	deg
δ_{ei}	−1.37	deg
h	1270	ft
m	1.59	slug
I_{yy}	4.65	slug-ft^2
S	5.90	ft^2
$\bar{c}$	0.915	ft

Table 2 T-2 nondimensional stability and control derivatives identified from flight test data.

Parameter	Estimate	Standard error
C_{Z_α}	−3.89	0.0272
C_{Z_q}	−5.28	2.1430
$C_{Z_{\delta_{eo}}}$	−0.180	0.0312
$C_{Z_{\delta_{ei}}}$	−0.163	0.0296
C_{m_α}	−1.29	0.0218
C_{m_q}	−38.0	1.7501
$C_{m_{\delta_{eo}}}$	−0.795	0.0260
$C_{m_{\delta_{ei}}}$	−0.817	0.0219

where δ_c is the commanded deflection and δ is the actual deflection. Sensor dynamics for transducers on the T-2 measuring the control surface deflections and aircraft responses were negligible over the bandwidth investigated. Gaussian white noise sequences were added to each of the measurements, where noise levels were identified from flight test data for the T-2 in calm air and are listed in Table 3.

Table 3 Measurement noise values for the T-2 simulation.

Measurement	Standard deviation	Unit
δ_{eo}	0.0313	deg
δ_{ei}	0.0307	deg
q	0.2337	deg/s
a_z	0.0042	g

B. X-56A MUTT Aeroelastic Demonstrator

The X-56A Multi-Use Technology Testbed (MUTT), shown in Fig. 2, is a subscale aeroelastic demonstrator designed for studying aeroelastic modeling and active flutter suppression technologies. The X-56A has a lambda-wing planform with stationary winglets. Two engines are mounted above the aft section of the center body. The landing gear are fixed and arranged in a tricycle configuration.

A planform view of relevant instrumentation and naming conventions for the X-56A is shown in Fig. 3. There are 10 control surfaces: four along the trailing edges of each wing and two along the trailing edges of the center body. The trailing-edge control surfaces are first designated with "bf" for body flap or "wf" for wing flap. The wing flaps are additionally annotated with a number that increases from wing root to wing tip. The designations end with "l" or "r" for left or right. For analysis of decoupled longitudinal motions, symmetric pairs of control surface deflections are denoted using the "s" subscript and defined, for example using the body flaps, as

$$\delta_{bfs} = \frac{1}{2}\left(\delta_{bfl} + \delta_{bfr}\right) \tag{11}$$

All control deflections are considered positive with trailing-edge down deflection and were measured using string potentiometers.

The X-56A is instrumented with 18 accelerometers: 4 longitudinal, 3 lateral, and 11 vertical. The embedded GPS/INS (EGI) installed near the nominal center of mass contains three of these accelerometers. The remaining

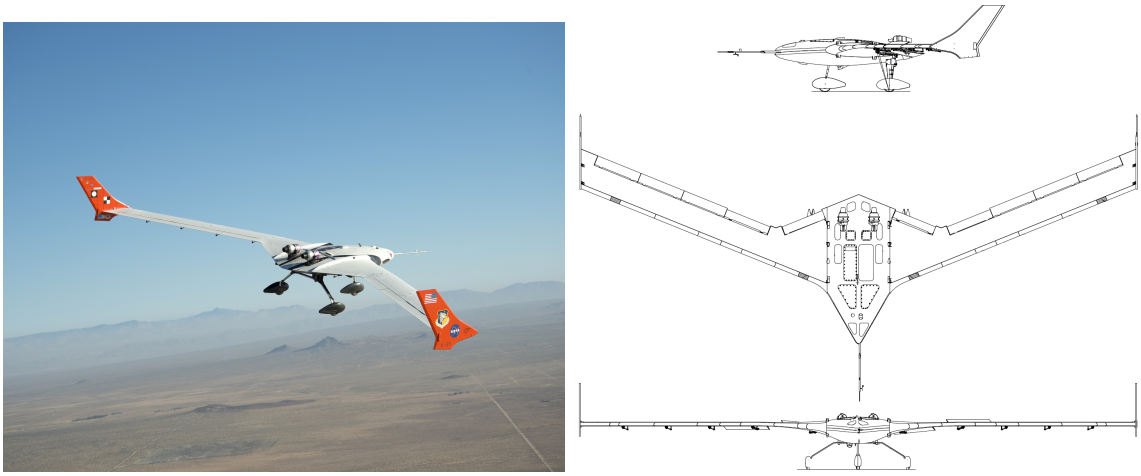

(a) Airplane in flight (credit: NASA / Jim Ross).

(b) Three-view drawing schematic.

Fig. 2 The X-56A MUTT subscale aeroelastic demonstrator.

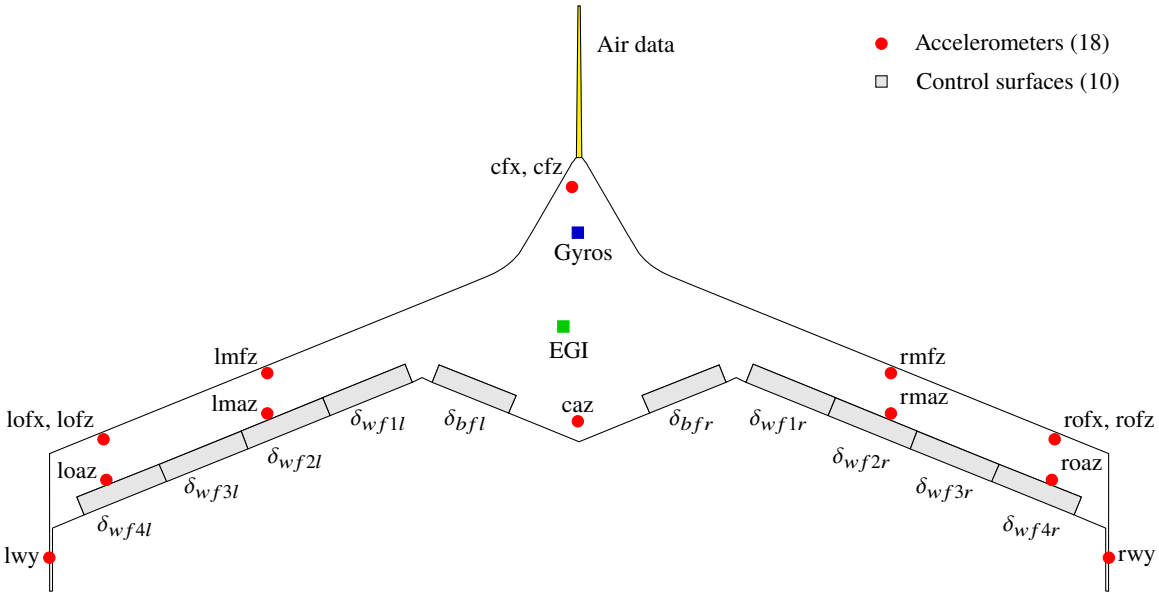

Fig. 3 X-56A planform with selected sensor and control surface locations.

center-body and wing accelerometers are designated first with an "*l*" for left wing, "*c*" for center body, or "*r*" for right wing; then "*w*" for winglet, "*o*" for outboard, or "*m*" for midspan; followed by "*f*" for forward, or "*a*" for aft. The last character is "*x*," "*y*," or "*z*" and designates the aircraft body axis in which the instrument is aligned.

The EGI also measures angular rates from a gyroscope and Euler angles. Additional high-rate gyroscopes are installed in the forward section of the center body. Air data vanes on the boom protruding from the nose measure angle of attack and flank angle. The nose boom also contains pressure ports, data from which were combined with temperature and pressure sensor readings to compute airspeed.

A computer-aided design (CAD) model and a finite element model (FEM), tuned to ground vibration test (GVT) data and tabulated for 25 structural modes at 17 fuel weights, were available. Measurements of fuel flow were combined with the CAD model and measured weights to model the aircraft mass properties and interpolate the structural modes during flight.

V. Method Development and Simulation Results

This section discusses frequency response estimates using the T-2 short period simulation. First, the open-loop case is considered, to demonstrate the method without feedback. Second, pitch rate feedback is used to close one loop and show degradation of the estimates when correlated secondary inputs are neglected, and then to show how to account for those inputs. Third, a case with multiple feedback loops is discussed to show the general procedure for computing the frequency responses in the presence of feedback.

Each of the following examples in this section use the same multisine input perturbations, design parameters for which are listed in Table 4. The duration for the excitation was $T = 20$ s, and the inputs contained uniformly-distributed power over the bandwidth 0.20–1.55 Hz in 0.05 Hz increments. In total, 28 frequencies were divided between the two inputs in an alternating manner so that each input contained 14 frequencies. The amplitudes of the inputs have been scaled to realistic values used in flight tests that have provided good data for modeling.

Table 4 Multisine design for the T-2 simulation, $T = 20$ s.

Outboard elevator $RPF = 1.01$			Inboard elevator $RPF = 1.07$		
a_k, deg	k	ϕ_k, rad	a_k, deg	k	ϕ_k, rad
0.6682	4	4.4689	0.6682	5	3.1810
0.6682	6	5.8120	0.6682	7	1.8081
0.6682	8	0.6209	0.6682	9	2.3098
0.6682	10	2.1651	0.6682	11	5.4763
0.6682	12	2.9535	0.6682	13	5.4012
0.6682	14	0.6831	0.6682	15	1.6265
0.6682	16	3.1888	0.6682	17	2.9788
0.6682	18	4.6742	0.6682	19	0.9953
0.6682	20	2.1209	0.6682	21	4.2239
0.6682	22	5.8333	0.6682	23	0.1763
0.6682	24	3.6763	0.6682	25	5.6324
0.6682	26	3.1250	0.6682	27	4.9781
0.6682	28	3.4605	0.6682	29	0.8641
0.6682	30	2.4622	0.6682	31	5.5661

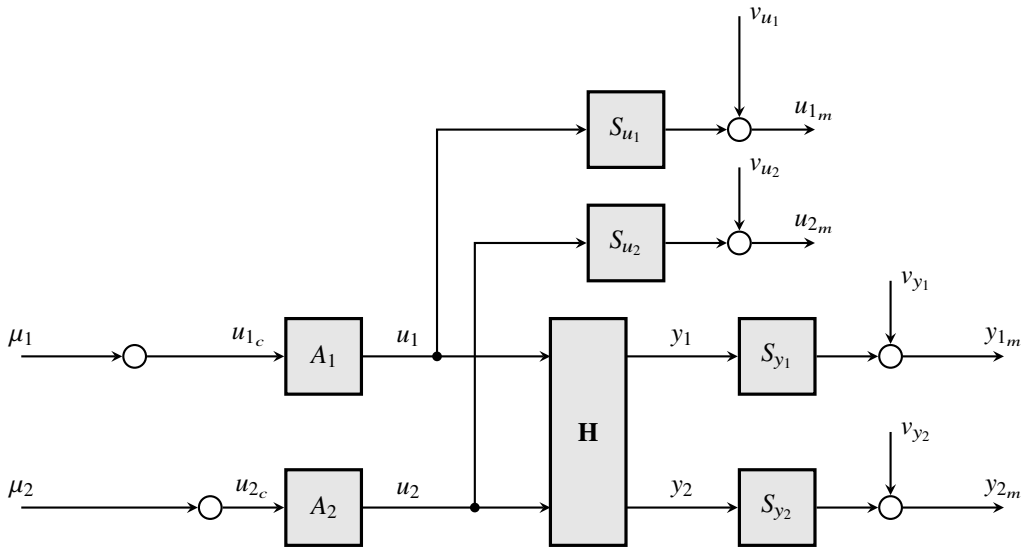

Fig. 4 Block diagram for the T-2 simulation in open-loop configuration.

A. Open Loop

The T-2 simulation was first excited using the multisine inputs while in the open-loop configuration without a control law. A block diagram for this setup is shown in Fig. 4. The nomenclature has been generalized for the block diagrams to more easily handle different scenarios. The signals μ_1 and μ_2 are the multisine perturbations added to the outboard and inboard elevator commands, respectively. Because there is no feedback or pilot commands in this example, these signals are also the commands u_{1_c} and u_{2_c} sent to the actuators A_1 and A_2. The actual control surface deflections u_1 and u_2 are input to the bare-airframe dynamics, represented as the frequency response matrix

$$\mathbf{H}(\omega) = \begin{bmatrix} H_{11}(\omega) & H_{12}(\omega) \\ H_{21}(\omega) & H_{22}(\omega) \end{bmatrix} = \begin{bmatrix} \frac{y_1(\omega)}{u_1(\omega)} & \frac{y_1(\omega)}{u_2(\omega)} \\ \frac{y_2(\omega)}{u_1(\omega)} & \frac{y_2(\omega)}{u_2(\omega)} \end{bmatrix} \tag{12}$$

and create output responses y_1 and y_2. Measured inputs and outputs, denoted by the additional "m" subscript, are observed using sensors having dynamics and additive measurement noise, e.g., S_{y_1} and v_{y_1}.

Measurements from a simulated maneuver are shown in Fig. 5(a). The multisines constructed using values in Table 4 are shown in the first two plots. These time histories had a pairwise correlation of 0.0, practically zero. The signal-to-noise ratios for all signals were high and the data perturbation sizes were similar to those in flight test maneuvers that produced good modeling results.

Fourier transform amplitudes of the measurements are shown in Fig. 5(b). The transforms were only evaluated at the 28 frequencies used in the multisine inputs because only these frequencies contain power in the steady-state response. In these plots, blue circles represent the multisine frequencies used for the outboard elevator, whereas red squares represent the multisine frequencies used for the inboard elevator. In this open-loop case, there are no secondary inputs and the entire spectra are only due to the respective primary inputs. In other words, δ_{eo} only contains power at the 14 frequencies in μ_1 (blue) and δ_{ei} only contains power at the 14 frequencies in μ_2 (red). The responses, however, have power at all of the 28 input frequencies. The slight difference in magnitude of the responses is due to the different values of control effectiveness for the two elevator surfaces. A slight attenuation of the control surface deflection amplitudes is present due to the actuator dynamics.

To compute the frequency responses from this data, consider the measurement of the i^{th} response, which can be expressed using block diagram algebra as

$$\begin{aligned} y_{i_m}(\omega) &= S_{y_i}(\omega) y_i(\omega) + v_{y_i}(\omega) \\ &= S_{y_i}(\omega) \left[H_{i1}(\omega) u_1(\omega) + H_{i2}(\omega) u_2(\omega) \right] + v_{y_i}(\omega) \\ &= S_{y_i}(\omega) \left[H_{i1}(\omega)\, S_{u_1}^{-1}(\omega) \left(u_{1_m}(\omega) - v_{u_1}(\omega) \right) + H_{i2}(\omega)\, S_{u_2}^{-1}(\omega) \left(u_{2_m}(\omega) - v_{u_2}(\omega) \right) \right] + v_{y_i}(\omega) \end{aligned} \tag{13}$$

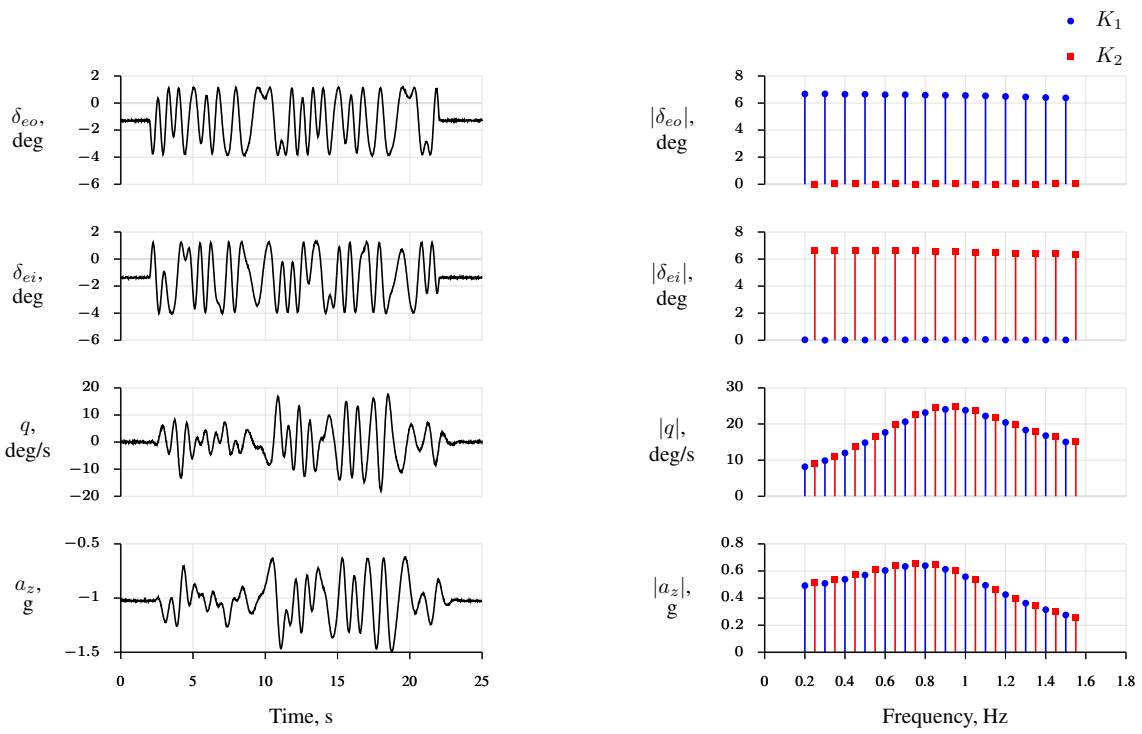

(a) Time histories.

(b) Fourier transform amplitudes.

Fig. 5 T-2 simulation data in the open-loop configuration.

Measurement noise or error in the sensor models can create errors in the frequency response measurements. However, sensors can typically be characterized well. If the sensors have sufficiently high bandwidths, those dynamics can be neglected. Furthermore, the multisines are typically designed so data will have high signal-to-noise ratios, and control surface deflections typically contain low levels of measurement noise. Although all these effects can be considered in the analysis, they can typically be neglected (which is done in the remaining development) so that $y_{i_m} \simeq y_i$ and $u_{j_m} \simeq u_j$, which simplifies the output measurement to

$$y_i(\omega) = H_{i1}(\omega)\, u_1(\omega) + H_{i2}(\omega)\, u_2(\omega) \tag{14}$$

In the steady-state response, the output only has power at the frequencies in the multisine excitation. Letting ω_1 and ω_2 represent any of the frequencies in K_1 and K_2, respectively, and evaluating the output in Eq. (14) at each set of frequencies generates a system of four linear equations

$$\begin{bmatrix} y_1(\omega_1) \\ y_2(\omega_1) \\ y_1(\omega_2) \\ y_2(\omega_2) \end{bmatrix} = \begin{bmatrix} u_1(\omega_1) & 0 & u_2(\omega_1) & 0 & 0 & 0 & 0 & 0 \\ 0 & u_1(\omega_1) & 0 & u_2(\omega_1) & 0 & 0 & 0 & 0 \\ 0 & 0 & 0 & 0 & u_1(\omega_2) & 0 & u_2(\omega_2) & 0 \\ 0 & 0 & 0 & 0 & 0 & u_1(\omega_2) & 0 & u_2(\omega_2) \end{bmatrix} \begin{bmatrix} H_{11}(\omega_1) \\ H_{21}(\omega_1) \\ H_{12}(\omega_1) \\ H_{22}(\omega_1) \\ H_{11}(\omega_2) \\ H_{21}(\omega_2) \\ H_{12}(\omega_2) \\ H_{22}(\omega_2) \end{bmatrix} \tag{15}$$

and eight unknown frequency response evaluations. The first two equations are the outputs evaluated at frequencies in K_1, whereas the second two equations are the outputs evaluated at frequencies in K_2. Together, these equations form the

fundamental linear algebra problem $\mathbf{Ax} = \mathbf{b}$. From the block diagram in Fig. 4, note that

$$u_1(\omega_2) = A_1(\omega_2)\mu_1(\omega_2) = 0 \tag{16a}$$

$$u_2(\omega_1) = A_2(\omega_1)\mu_2(\omega_1) = 0 \tag{16b}$$

because each control surface only contains frequencies from the corresponding primary input, by design and as shown in Fig. 5(b). Substituting this result into Eq. (15) eliminates four of the unknown frequency response evaluations and reduces the system of equations to

$$\begin{bmatrix} y_1(\omega_1) \\ y_2(\omega_1) \\ y_1(\omega_2) \\ y_2(\omega_2) \end{bmatrix} = \begin{bmatrix} u_1(\omega_1) & 0 & 0 & 0 \\ 0 & u_1(\omega_1) & 0 & 0 \\ 0 & 0 & u_2(\omega_2) & 0 \\ 0 & 0 & 0 & u_2(\omega_2) \end{bmatrix} \begin{bmatrix} H_{11}(\omega_1) \\ H_{21}(\omega_1) \\ H_{12}(\omega_2) \\ H_{22}(\omega_2) \end{bmatrix} \tag{17}$$

which is a fully determined having the solution

$$\begin{bmatrix} H_{11}(\omega_1) \\ H_{21}(\omega_1) \\ H_{12}(\omega_2) \\ H_{22}(\omega_2) \end{bmatrix} = \begin{bmatrix} \frac{1}{u_1(\omega_1)} & 0 & 0 & 0 \\ 0 & \frac{1}{u_1(\omega_1)} & 0 & 0 \\ 0 & 0 & \frac{1}{u_2(\omega_2)} & 0 \\ 0 & 0 & 0 & \frac{1}{u_2(\omega_2)} \end{bmatrix} \begin{bmatrix} y_1(\omega_1) \\ y_2(\omega_1) \\ y_1(\omega_2) \\ y_2(\omega_2) \end{bmatrix} \tag{18}$$

More generally, the solution is also

$$H_{ij}(\omega_j) = \frac{y_i(\omega_j)}{u_j(\omega_j)} \tag{19}$$

which is the ratio of output and input Fourier transforms at the frequencies contained in the corresponding input. Equation (19) is applied for each harmonic in the input and the MIMO frequency responses are computed at the corresponding frequencies. Specifically for this example, the $\mathbf{A}$ matrix has 56×56 elements because there are two inputs, two outputs, and 14 frequencies per input.

Computing frequency responses in this manner has several advantages. The analysis is straightforward and does not require tuning or using engineering judgement to select arbitrary parameters in the calculations. It is applicable to MIMO systems and is simple enough to run in real time during flight with limited computational resources. For good signal-to-noise ratios and sufficient time durations, these estimates of the frequency response are accurate and unbiased.

Frequency response estimates for the simulation data are shown in Fig. 6. The plots in the left column, shown with blue circles, had the outboard elevator as input and were computed at harmonics in K_1. Likewise, the plots in the right column, shown with red squares, correspond to the inboard elevator input and were computed at the harmonics in K_2. These estimates were accurate and were practically equal to the known true frequency responses of the bare-airframe dynamics, shown as a solid black line over the excitation bandwidth. The effects of noise were small. The dashed purple lines, which also fell on the true frequency responses, are the solutions of using the output-error approach to match time histories of the measured responses [1, 14] using Eq. (7) as the parametric model.

B. Single Loop Closure

In this second example, the pitch rate output was fed back to the inboard elevator, as shown by the block diagram in Fig. 7. This setup has been used with the T-2 aircraft to mimic aircraft damage and faults. The control gain $K = -0.2$ was used to move the short period pole from $\lambda = -2.56 \pm 5.34j$ ($\omega_n = 5.92$ rad/s, $\zeta = 0.43$) to $\lambda = -4.88 \pm 5.09j$ ($\omega_n = 7.05$ rad/s, $\zeta = 0.69$) which increased the frequency and damping. In general, the feedback block K can also model other effects, such as low-pass filters applied to the sensor measurements.

Simulated measurements for this maneuver are shown in Fig. 8(a). The outboard elevator is the same as in the previous example, whereas the feedback changed the inboard elevator. The correlation between the two control surface deflections rose to 0.4. While this correlation is much less than the maximum 0.9 guideline typically used for other estimation methods such as output error [1], it is a large increase from the open-loop example. The pitch rate and vertical acceleration time histories are also different in form and smaller in amplitude than in the previous example due to the different inboard elevator waveform.

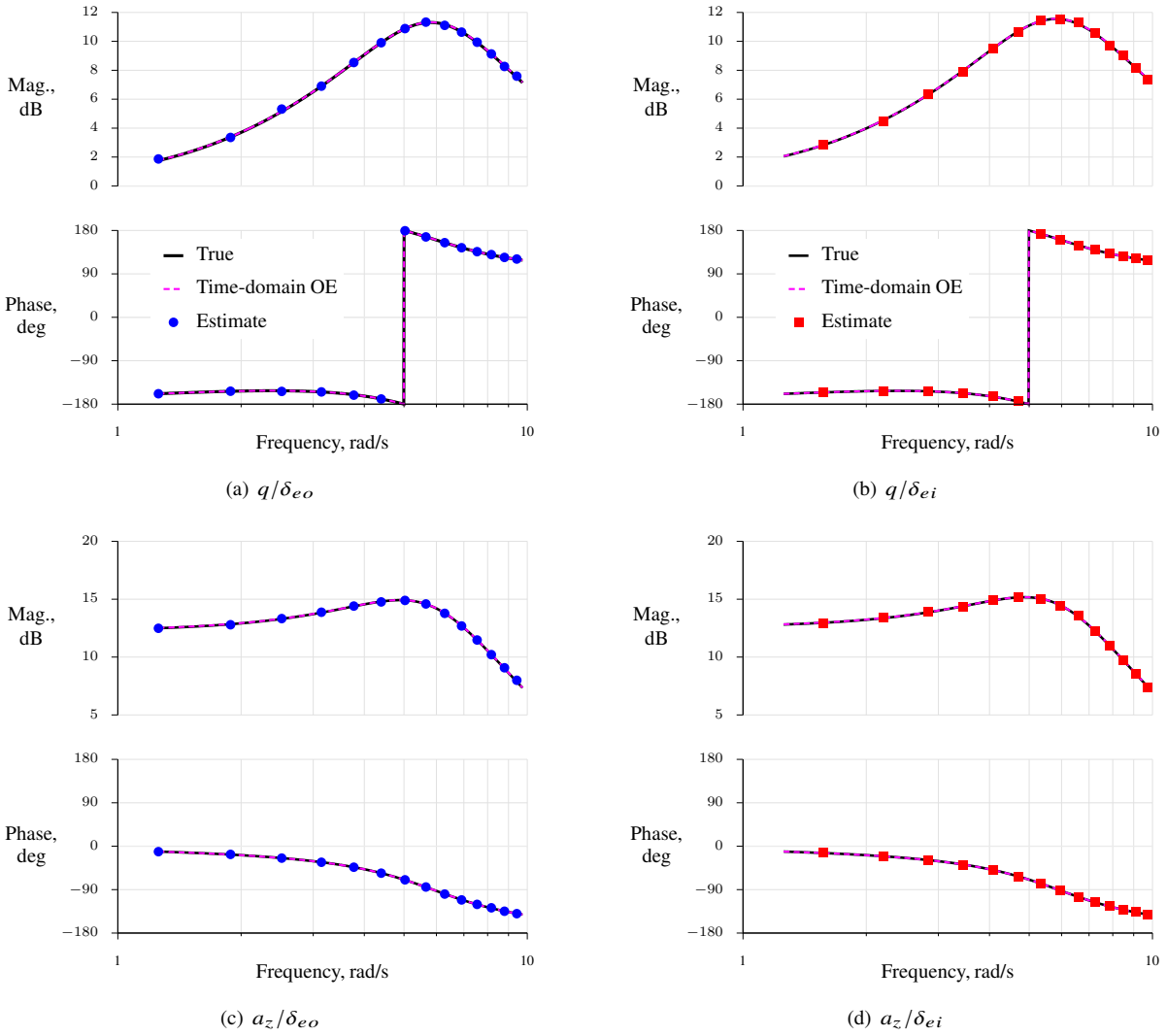

Fig. 6 Frequency response estimates as Bode plots for T-2 simulation in open-loop configuration.

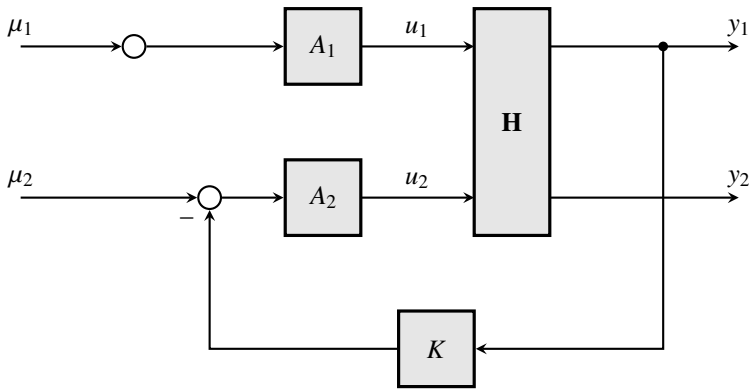

Fig. 7 Block diagram for the T-2 simulation with one loop closure.

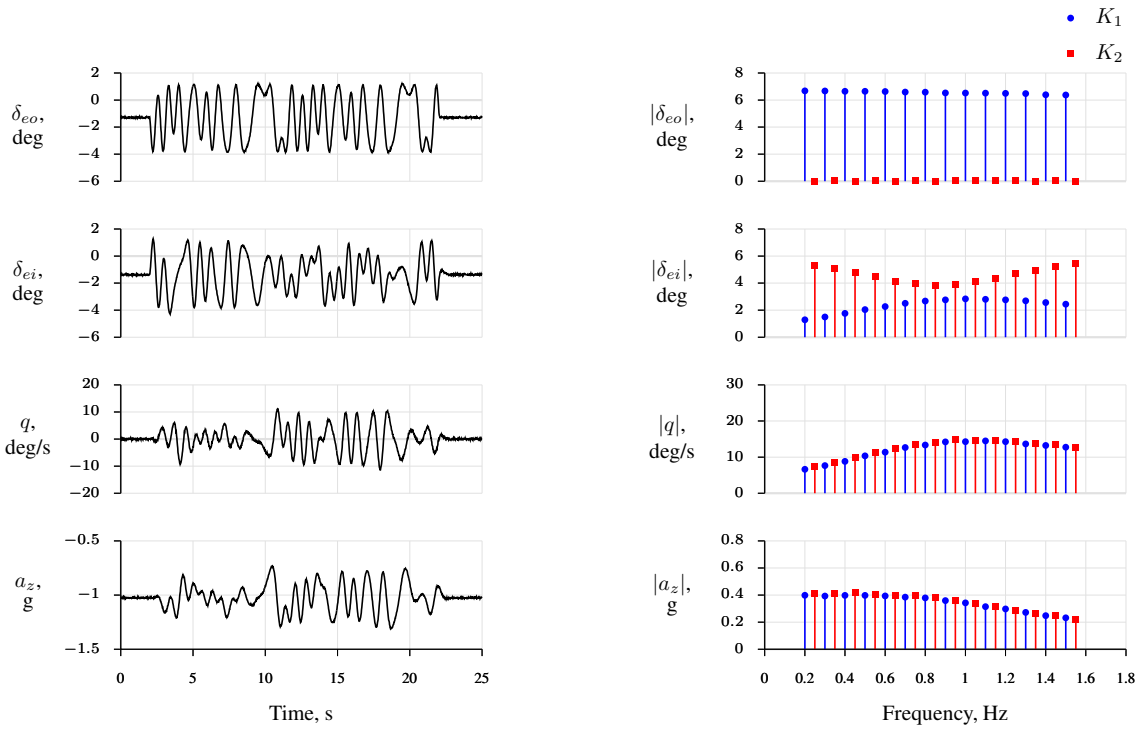

(a) Time histories.

(b) Fourier transform amplitudes.

Fig. 8 T-2 simulation data with one loop closure.

The corresponding Fourier transforms of the data are shown in Fig. 8(b). The amplitudes of the pitch rate and vertical acceleration are lower than in Fig. 5(b). The outboard elevator is the same as before, but the inboard elevator is smaller in amplitude and decreases near the short period frequency. For estimating frequency responses from this data, it is important that the inboard elevator contained significant power at frequencies in the outboard elevator multisine, shown as blue circles. The small amount of feedback led to relatively large secondary inputs in the inboard elevator. The effects of these correlated secondary inputs on the frequency response estimates are examined next.

To compute frequency responses from this data, the i^{th} measurement is expanded as in Eq. (15). Due to the feedback,

$$u_1(\omega_2) = A_1(\omega_2)\mu_1(\omega_2) = 0 \tag{20a}$$

as before, but now

$$\begin{aligned} u_2(\omega_1) &= A_2(\omega_1)\left[\mu_2(\omega_1) - K(\omega_1)y_1(\omega_1)\right] \\ &= -A_2(\omega_1)K(\omega_1)y_1(\omega_1) \end{aligned} \tag{20b}$$

because responses excited by the outboard elevator and containing all 28 frequencies are being fed back to the inboard elevator. In this case, the frequency responses from the second input (containing the feedback) are

$$H_{i2}(\omega_2) = \frac{y_i(\omega_2)}{u_2(\omega_2)} \tag{21a}$$

as in Eq. (19) for the open-loop case, but the frequency responses from the first input (not containing the feedback) are

$$H_{i1}(\omega_1) = \frac{y_i(\omega_1)}{u_1(\omega_1)} - \frac{H_{i2}(\omega_1)\,u_2(\omega_1)}{u_1(\omega_1)} \tag{21b}$$

which have additional contributions than in the open-loop case arising from the feedback and dependent upon $H_{i2}(\omega_1)$. Because only $H_{i2}(\omega_2)$ was computed in Eq. (21a), additional information is needed to determine $H_{i2}(\omega_1)$. One approach

is to fit the frequency response data H_{i2} at frequencies in K_2 with a parametric model using the method described in Ref. [15], and then resample the identified frequency response at frequencies in K_1. Another approach is to interpolate the identified $H_{i2}(\omega_2)$ from multiple frequencies in K_2 to obtain $H_{i2}(\omega_1)$, and use that information to then compute $H_{i1}(\omega_1)$. Viewed another way, substituting the result from Eq. (20) into (15) creates an underdetermined linear system with four equations and six unknown frequency response evaluations. Adding two additional linear interpolation equations expressing $H_{i2}(\omega_1)$ in terms of $H_{i2}(\omega_2)$ makes the system fully determined. For example, two multisines with alternating frequencies, as in this example, have linear interpolation equations that simplify to

$$0 = H_{i1}(\omega_{11}) + H_{i1}(\omega_{12}) - 2H_{i1}(\omega_{21}) \tag{22}$$

where ω_{11} and ω_{12} are two neighboring frequencies in K_1 spanning ω_{21} in K_2. If the frequency resolution is coarse and the frequency response has sharp peaks, this approach could introduce errors. However, given an adequate multisine design, the frequency resolution should be sufficient to obtain accurate results.

If the frequency responses were computed for this example using only Eq. (19), which was developed for the open-loop case, then $H_{i2}(\omega_2)$ is correct but $H_{i1}(\omega_1)$ is incorrect. This was demonstrated in Ref. [5] and is a result of neglecting the second term in the right side of Eq. (21b). If the effects of feedback are properly considered, for example using the interpolation just described, the bare-airframe dynamics may be accurately computed from closed-loop data.

Frequency response estimates using the simulation data are shown in Fig. 9. Interpolated points were discarded and not shown. For compatibility with the results in the following section containing multiple loop closures, a simple linear interpolation scheme was used. A slightly better fit was obtained using a cubic interpolation, but this approach does not work well in the general case discussed in the next section. Estimates computed using the correct procedure, shown as solid markers, fell on the true bare-airframe frequency responses. The open-loop estimates, shown as open markers, are incorrect for frequency responses with δ_{eo} (not containing feedback) and correct with δ_{ei} (containing feedback). Results using output error to fit time-domain measurements also matched the true frequency responses because the control surface correlations were much less than 0.9.

In general, as feedback gains increase, the open-loop and closed-loop frequency responses become more different and the errors incurred from not accounting for secondary inputs become larger. However, as shown in this example, even small amounts of feedback can lead to significant errors in the frequency response estimates. The analysis becomes more sensitive to these secondary inputs when there are fewer inputs because each input impacts a larger fraction of the total response. It is perhaps counter-intuitive that the frequency responses for the input without feedback are the ones that are incorrect using the open-loop approach.

C. Multiple Loop Closures

In this example, pitch rate was fed back to both the outboard and the inboard elevators, as shown in the block diagram in Fig. 10. The control gain

$$\mathbf{K} = \begin{bmatrix} K_{11} \\ K_{21} \end{bmatrix} = \begin{bmatrix} -0.1 \\ -0.1 \end{bmatrix} \tag{23}$$

was used to move the short period pole from $\lambda = -2.56 \pm 5.34j$ ($\omega_n = 5.92$ rad/s, $\zeta = 0.43$) to $\lambda = -4.84 \pm 5.10j$ ($\omega_n = 7.03$ rad/s, $\zeta = 0.69$), similar to the previous case with one loop closure. This setup has also been flown on the T-2 aircraft to test control laws.

Simulated measurements for this maneuver are shown in Fig. 11(a). The control surface deflections, which now both contain pitch-rate feedback, had a pairwise correlation of 0.3 which is again far less than the maximum 0.9 guideline. The correlation was less than in the previous case because the feedback was decreased. The pitch rate and vertical acceleration outputs have approximately the same magnitude as the previous case, which was expected because roughly the same closed-loop dynamics were achieved by the feedback.

Fourier transforms of the measurements are shown in Fig. 11(b). Both control surfaces now exhibit reduced amplitudes relative to the open-loop case, decreases in amplitudes near the short period frequency, and mixing of the multisine frequencies due to the feedback. For δ_{ei}, the secondary amplitudes resulting from the feedback are half of those shown in the previous case because the control gain was halved. The spectra for the pitch rate and vertical acceleration are approximately the same as in the previous case.

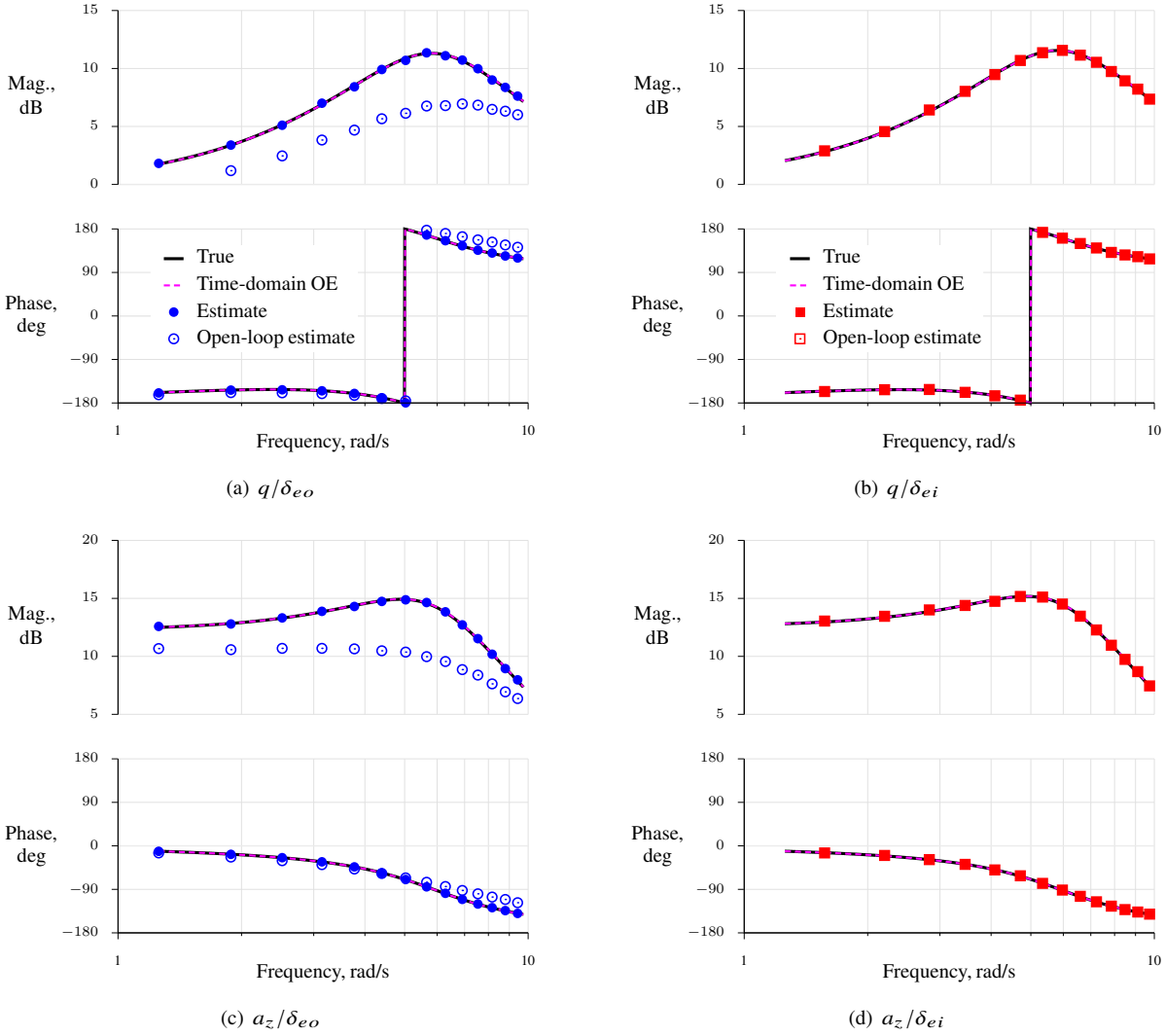

Fig. 9 Frequency response estimates as Bode plots for T-2 simulation with one loop closure.

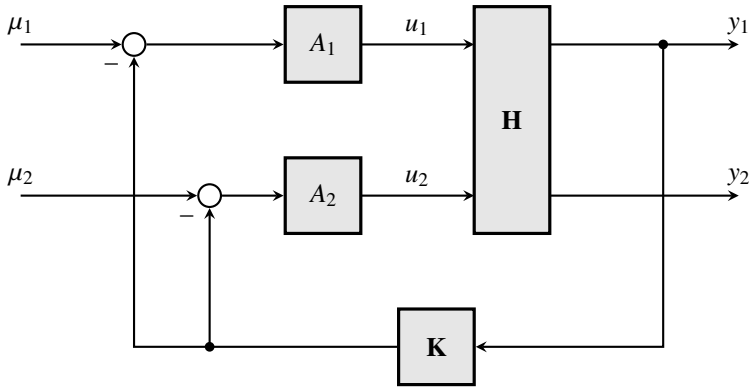

Fig. 10 Block diagram for the T-2 simulation with multiple loop closures.

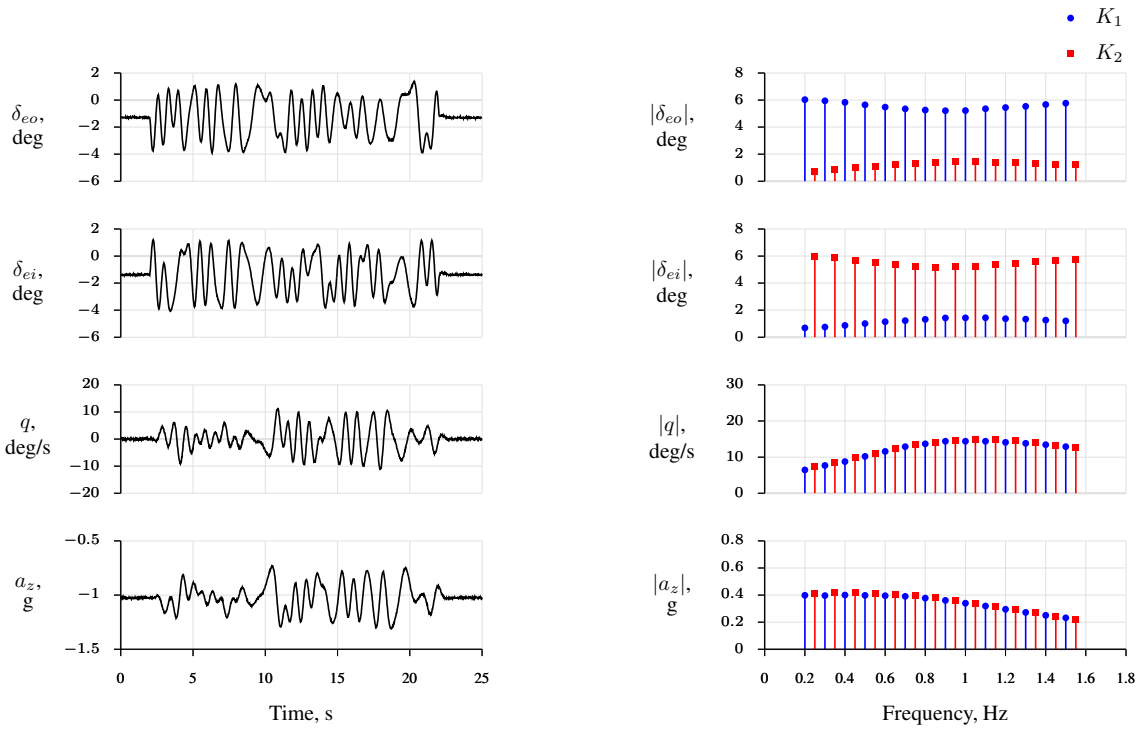

(a) Time histories.

(b) Fourier transform amplitudes.

Fig. 11 T-2 simulation data and Fourier transforms with multiple loop closures.

Output measurements were again expanded as in Eq. (15). In this case, the secondary inputs evaluate as

$$\begin{aligned} u_1(\omega_2) &= A_1(\omega_2)\left[\mu_1(\omega_2) - K_{11}(\omega_2)y_1(\omega_2)\right] \\ &= -A_1(\omega_2)K_{11}(\omega_2)y_1(\omega_2) \end{aligned} \tag{24a}$$

$$\begin{aligned} u_2(\omega_1) &= A_2(\omega_1)\left[\mu_2(\omega_1) - K_{21}(\omega_1)y_1(\omega_1)\right] \\ &= -A_2(\omega_1)K_{21}(\omega_1)y_1(\omega_1) \end{aligned} \tag{24b}$$

which are both non-zero due to the feedback. The primary frequency response evaluations are

$$H_{i1}(\omega_1) = \frac{y_i(\omega_1)}{u_1(\omega_1)} - \frac{H_{i2}(\omega_1)\,u_2(\omega_1)}{u_1(\omega_1)} \tag{25a}$$

$$H_{i2}(\omega_2) = \frac{y_i(\omega_2)}{u_2(\omega_2)} - \frac{H_{i1}(\omega_2)\,u_1(\omega_2)}{u_2(\omega_2)} \tag{25b}$$

which now both contain contributions from correlated secondary inputs. Unlike when only one loop was closed, one frequency response can not be computed first and then substituted into the remaining equations; rather, more information must be provided from interpolation and the entire set of unknown frequency responses solved for simultaneously.

The frequency response estimates are shown in Fig. 12. Estimates using the correct closed-loop procedure and those from an identified model using the traditional output-error approach matched the true frequency responses. The traditional output-error results were not affected by the feedback because the pairwise correlation was lower than 0.9. The open-loop estimates of the frequency responses were in error because the additional terms due to the feedback were neglected, making each frequency response estimate incorrect. The amount of this error is less than in the previous case because the feedback gains were lower.

For this example, the $\mathbf{A}$ matrix becomes a square 56×56 element matrix. This system of equations was solved in MATLAB® on a standard laptop in under 0.003 s. This would be fast enough to perform a real-time analysis for several

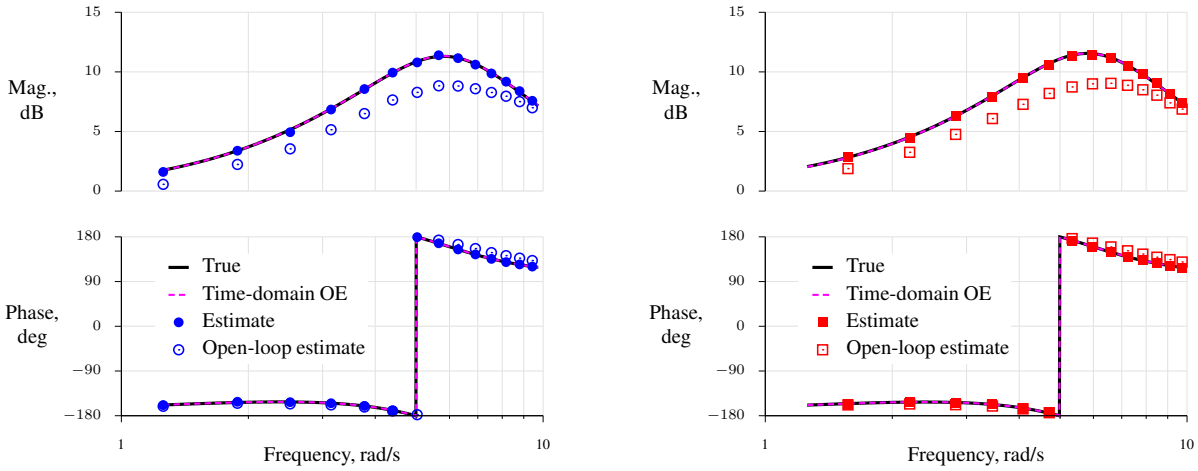

(a) q/δ_{eo} (b) q/δ_{ei}

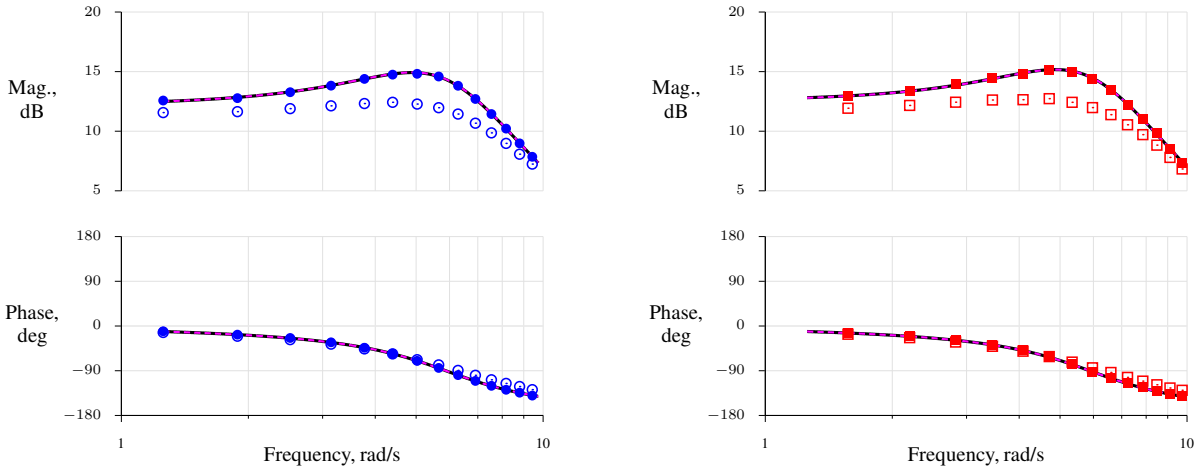

(c) a_z/δ_{eo} (d) a_z/δ_{ei}

Fig. 12 Frequency response estimates as Bode plots for T-2 simulation with multiple loop closures.

inputs and outputs using standard aircraft research instrumentation and rigid-body dynamics. As data are recorded, Fourier transforms would be updated using Eq. (6). Then, perhaps at a slower update rate, the matrices in Eq. (15) would be populated and solved for the frequency response estimates.

For the simulation data used in this example, estimated frequency responses were also accurate when fewer multisine frequencies were used. Because the frequencies are harmonic multiples, they can be arbitrarily discarded without affecting the analysis at other frequencies. When all but 5 frequencies from the available 14 frequencies on each input were discarded, only slight variations in the frequency response estimates were observed. For the output error analysis, the estimated parameters were approximately the same but the standard errors were larger due to reduced frequency content and less data information.

VI. Flight Test Results

In this section, results using flight test data from the X-56A aircraft are presented. The maneuver is from Phase 1 and Flight 18 with multisine input FTA 506. The airspeed was at approximately 80% of the predicted flutter speed and the mean fuel was at 32% capacity.

A block diagram of the simplified longitudinal closed-loop system dynamics for this maneuver, including a control law for gust load alleviation (GLA), is shown in Fig. 13. The pilot longitudinal stick commanded the flight path angle γ. The error in the flight path angle was passed through a PID control law to command the pitch rate. The pitch rate error was combined with a feed-forward and PI control law and passed through a structural filter before forming a (virtual) elevator command, which was sent to the δ_{wf2s} and δ_{wf3s} surface pairs. The block $K_{ele,q}$ contained a pitch gyro filter and a notch filter for removing the second symmetric wing bending mode. The center forward vertical acceleration was fed back through a band-pass filter and a gain to the δ_{bfs} surface pairs. The (virtual) symmetric bending acceleration was computed as

$$a_z^{sb} = \frac{1}{4}\left(a_z^{lof} + a_z^{rof} + a_z^{loa} + a_z^{roa}\right) - 0.7\, a_z^{cf} \tag{26}$$

and was fed back through a band-pass filter and two gains to the δ_{bfs} and δ_{wf4s} control surface pairs. Multisine inputs were added to the actuator commands after the control mixing and feedback. Sensor dynamics were negligible for the bandwidth examined in this maneuver.

The excitation inputs for this maneuver included five multisines for exciting symmetric pairs of control surface deflections. In total, 325 frequencies were applied, with 65 on each of the 5 control surface pairs. The pairwise correlations of the control surface measurements were at most 0.1 for this maneuver. Time histories are shown in Fig. 14(a) for one cycle of the input (the full maneuver contained about 2.5 cycles of excitation), where each y-axis contains the same range but different mean value. Fourier transform amplitudes of these data, evaluated at the multisine frequencies, are shown in Fig. 14(b) where the colors are again used to differentiate the multisine frequencies. The pilot flight path command and throttle settings were approximately constant through the maneuver. The multisines spanned the short period and four structural modes which are illustrated in Fig. 15 using the FEM. The multisines were designed with uniform power spectra. The actuator dynamics created a roll-off with increasing frequency. The effects of mixing and feedback were most prominent in δ_{wf2s} and δ_{wf3s} near the short period mode, and in δ_{bfs} and δ_{wf4s} near the first symmetric wing bending mode, where the amplitudes from the primary frequencies diminished and where there was increased content from secondary input frequencies.

Output response data measurements selected for modeling are shown in Fig. 16(a), over the same time scales as in Fig. 14(a), and Fourier transforms are shown in Fig. 16(b). The modeling outputs were sensor measurements or combinations of sensor measurements and not exactly the variables used for feedback shown in Fig. 13. The aircraft responses were small perturbations about the reference flight condition. As shown most clearly by the Fourier transform data, the short period, SW1B, and SW1T modes were excited by the inputs. There was also some excitation of the SWL mode, but the excitation bandwidth ended lower than the SWL resonant frequency. For the wing accelerometer measurements, the "s" denotes a symmetric averaging over measurements from the left and right wings, for example

$$a_z^{smf} = \frac{1}{2}\left(a_z^{lmf} + a_z^{rmf}\right) \tag{27}$$

The input and output data were transformed into the frequency domain at the frequencies contained in the multisine inputs. Simple approximations were then used to estimate and remove time skews from Fourier transforms of the output response data and scale factor errors for the angle of attack and pitch rate measurements [3, 16]. These corrections to the data were small but important and improved the estimated frequency responses. Time skews between the control surface

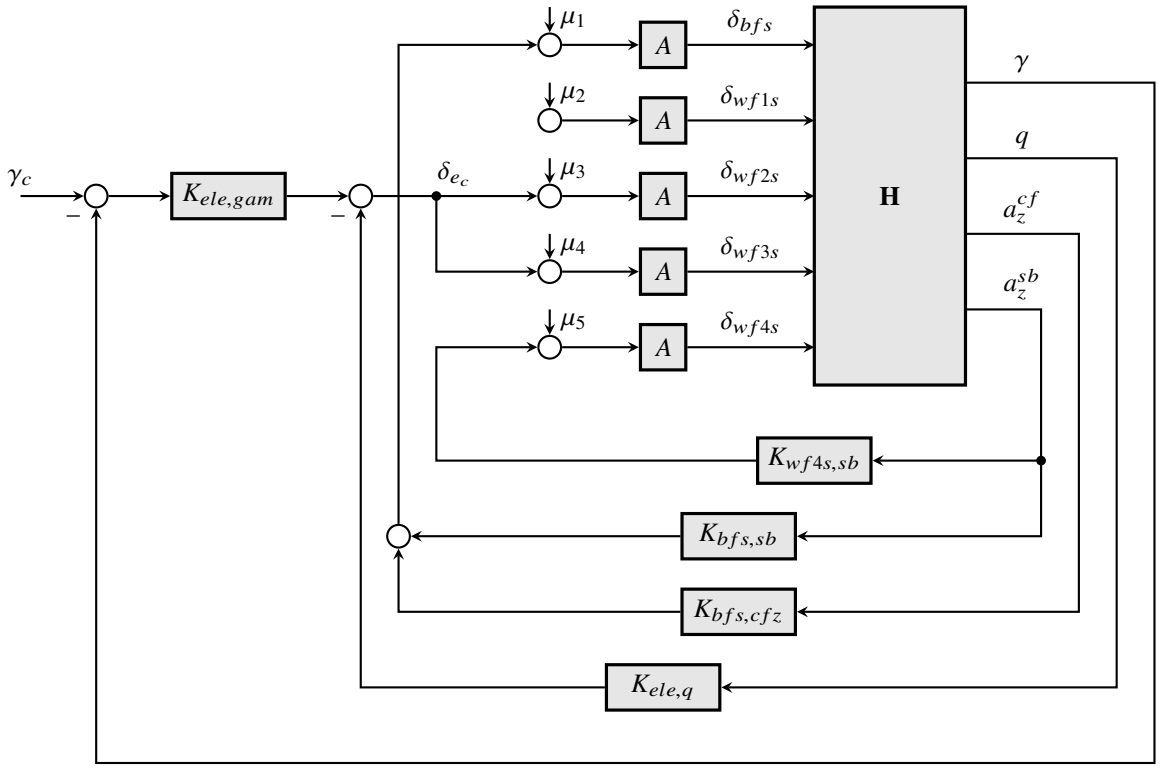

Fig. 13 Simplified block diagram for the X-56A gust load alleviation control law.

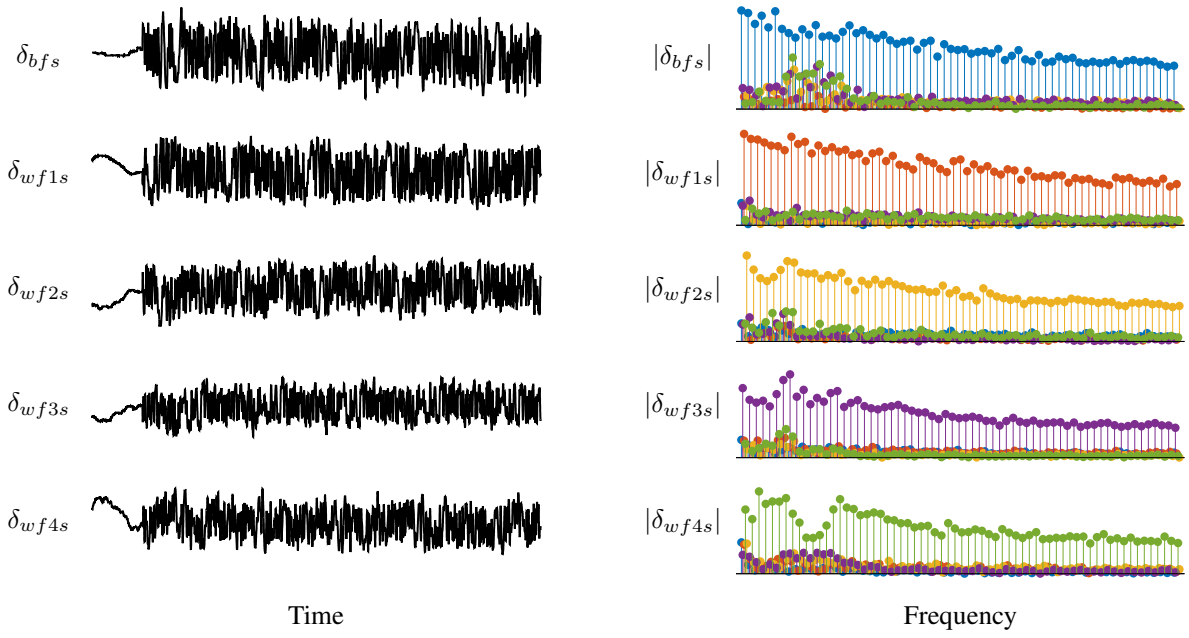

(a) Time histories.

(b) Fourier transform magnitudes.

Fig. 14 X-56A measured input data.

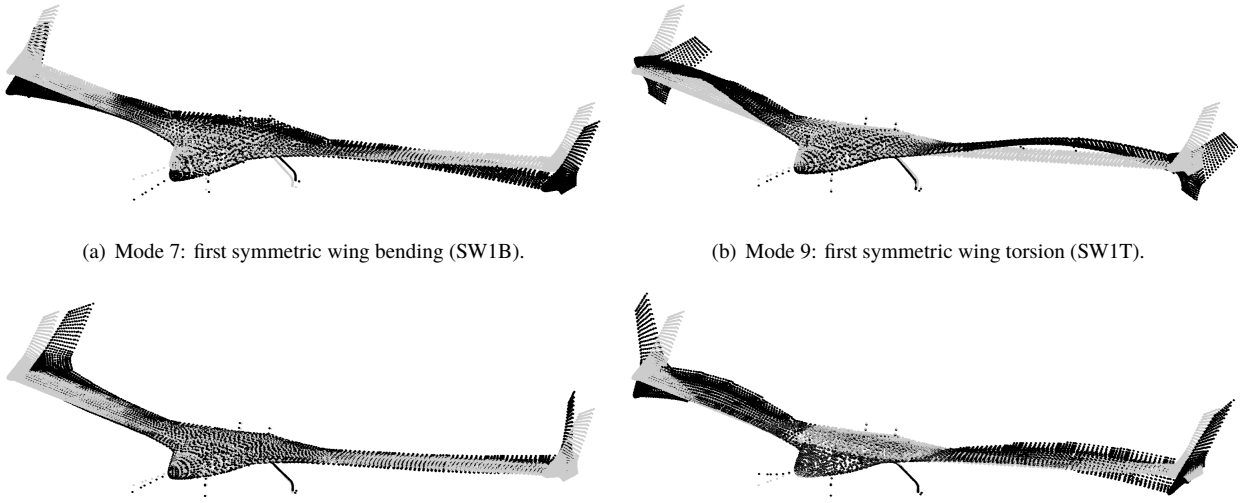

(a) Mode 7: first symmetric wing bending (SW1B).

(b) Mode 9: first symmetric wing torsion (SW1T).

(c) Mode 10: symmetric wing fore-aft (SWFA).

(d) Mode 14: symmetric winglet lateral (SWL).

Fig. 15 Longitudinal mode shapes for the X-56A flight data (FEM configuration 24611, version 10.424_dev, 50% fuel). Gray markers are the undeformed grid points and black markers are the deformed points.

deflection measurements and the synchronized output responses, which arose from measuring the data on different data buses, were estimated at the same time as the nondimensional stability and control derivatives, discussed later.

The frequency responses were then estimated using the general procedure described in Section V.C. The entire input-output data set was corrected at once, instead of breaking the problem into smaller parts, resulting in an **A** matrix from Eq. (15) that had 16250×16250 elements (5 inputs, 10 outputs, and 325 frequencies). Application of the "sparse matrix" variable type in MATLAB® produced solutions in under 0.05 s on a standard laptop computer, which could still be used for real-time estimation. For comparison, solving the system using standard double-precision variables used 94 s, three orders of magnitude longer in duration.

Frequency response estimates for the q/δ_{wf4s} and a_z^{ca}/δ_{wf4s} transfer functions are shown in Fig. 17(a) as Bode plots. These frequency responses were ones that, due to the bare airframe dynamics, had high signal-to-noise ratios over most of the input bandwidth. Estimates for all other transfer functions are shown as Bode magnitude plots in Fig. 18. The color of each set of estimates indicates the corresponding multisine input, consistent with Figs. 14(b) and 16(b). As before, the solid markers are the correct frequency response estimates, whereas the open markers are the open-loop estimates. The black lines are fits to the corrected frequency response estimates using output error, as discussed in Ref. [15], and a parametric model based on nondimensional stability and control derivatives. The dashed purple lines, taken from Ref. [17], are the frequency responses estimated from the same input-output data and parametric model, but using output error to match Fourier transforms of measured responses (rather than time histories, as in the simulation results). Observations for the selected Bode plots in Fig. 17 generally extend to the results shown in Fig. 18. Some of the responses in Fig. 18, such as the α/δ_{bfs} had low sensitivity and signal-to-noise ratios. This could be due to low sensitivity in the aircraft dynamics or because the body flaps are in the wake of the jet engines. In future maneuvers, amplitudes of the inboard flaps could be increased to achieve higher signal-to-noise ratios. Using this data in the output error parameter estimation did not significantly change parameter estimates, but rather increased the standard errors, which were relatively low. In other results, small mismatches could be due to the truncated aeroelastic modes (even at lower frequencies, due to couplings) and/or errors in FEM mode shapes substituted in the estimation.

Examining the Bode plots in Fig. 17(a), the corrections had little effect on many of the frequency response points. As expected, the main differences were near the short period and SW1B modes where most of the mixing and control activity was present. These corrections were important because the apparent character of the frequency responses changed from a single combined mode at an intermediate frequency to two distinct (short period and SW1B) modes at higher and lower frequencies. Errors in computing the frequency responses using the open-loop calculations would have led to incorrect assessments of the modal frequency and damping ratios, which were being used to update simulations

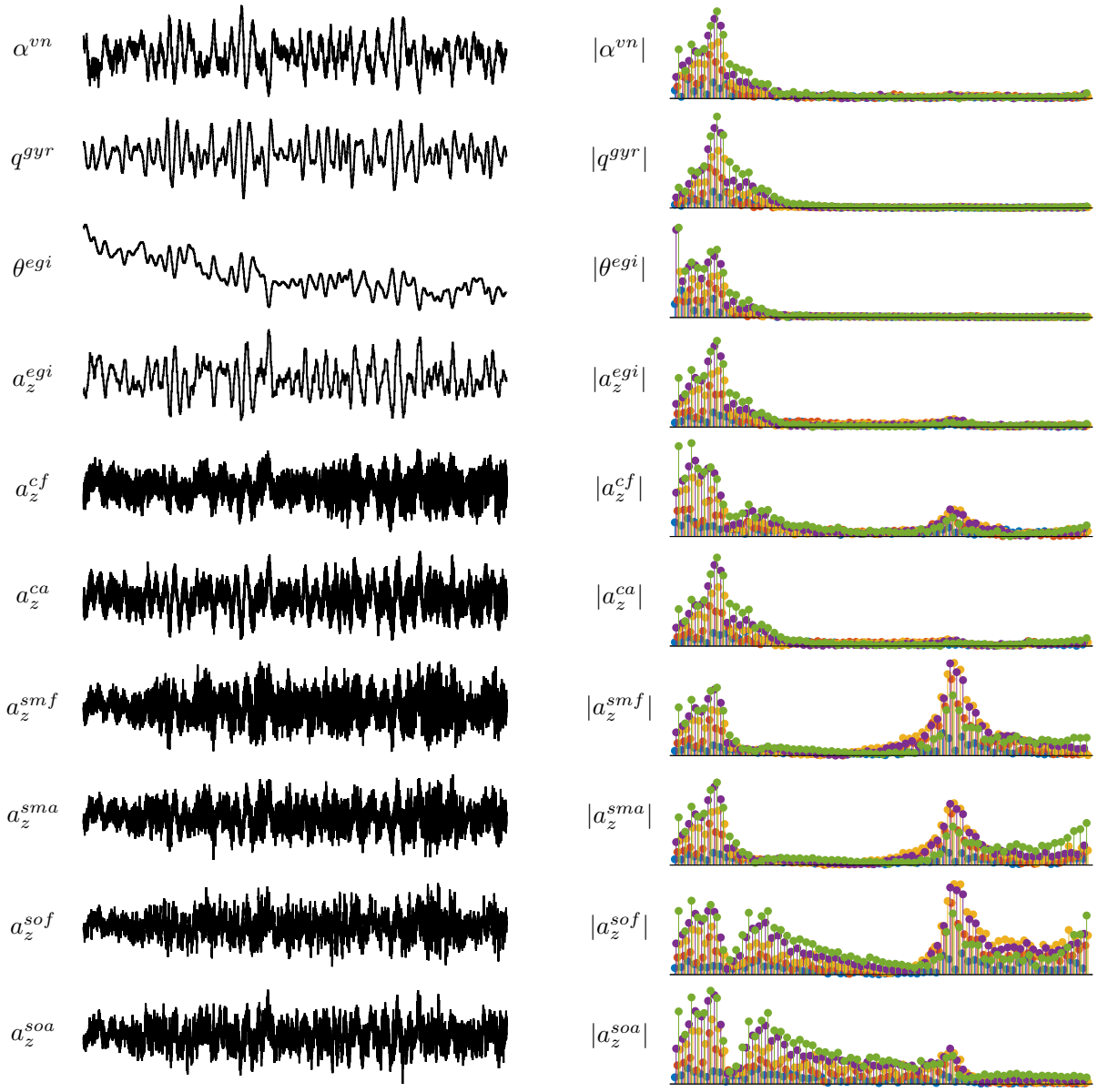

(a) Time histories.

(b) Fourier transform magnitudes.

Fig. 16 X-56A measured output data.

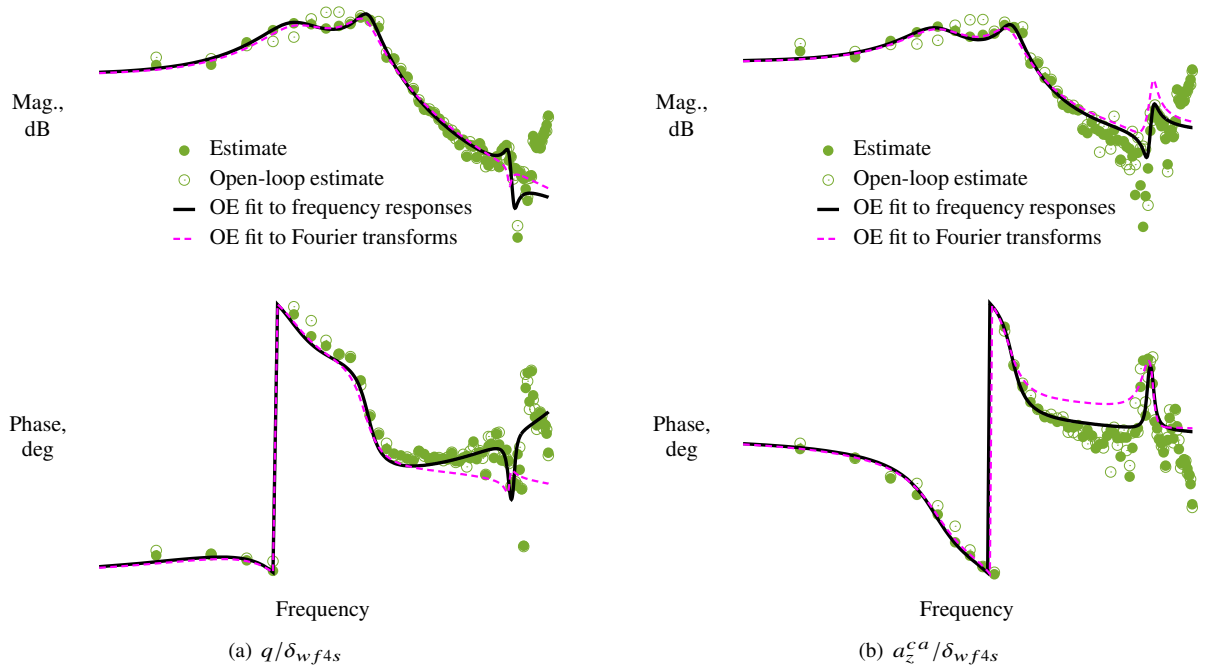

(a) q/δ_{wf4s} (b) a_z^{ca}/δ_{wf4s}

Fig. 17 Frequency response estimates as Bode plots for X-56A flight test data.

of the X-56A and tune control laws.

The parametric modeling results, shown in black and purple, considered the short period, SW1B, and SW1T modes. These identified models were in agreement with the frequency response data and each other. For output error fitting the frequency response data directly, time skews between the input and response measurements were removed by estimating a time delay on each input-output channel. This also approximated phase lags due to higher-order structural modes such as SWL not considered in the model structure [3]. For output error fitting Fourier transforms, a single delay was used to account for the time skew between the data bus containing the input measurements and the data bus containing the output measurements. Otherwise the model structure and modeling data were the same. As presented in Ref. [17], models fitting Fourier transforms matched the flight data well, had good predictive capability for maneuvers with different types of input excitation and aeroelastic modes resulting from differences in airspeed and fuel weight, and accurately characterized the aeroelastic instability at higher airspeeds. Similar results were obtained from these two methods, which used different modeling data, because an adequate model structure was used with good quality data. Specifically, the fitted frequency response data were corrected for secondary correlated inputs, and the fitted Fourier transform data had pairwise input correlations of less than 0.1, which were low. These two independent results therefore support an accurate identification of the X-56A bare airframe dynamics from closed-loop flight test data.

VII. Conclusions

A method was developed for computing multiple-input multiple-output frequency response estimates when the inputs include orthogonal phase-optimized multisines and correlated inputs arising from control mixing or feedback control. An earlier approach based on dividing Fourier transforms of measured output by input data at the frequencies in the multisine inputs was extended to include the effects of these secondary inputs. This formulation led to an underdetermined system of linear equations. The system was made fully determined by including linear interpolations of the frequency responses between the multisine frequencies. The method was demonstrated using simulation data in open loop and with single and multiple loops closed by a control law. The method was also demonstrated using flight test data from the X-56A airplane flying under closed-loop control with control mixing.

Techniques for system identification break down as inputs become highly correlated because estimators cannot uniquely attribute responses to the individual inputs. This is a data information issue and not specific to any method. For output error, it is important to have input correlations less than 0.9. For the proposed method of frequency response

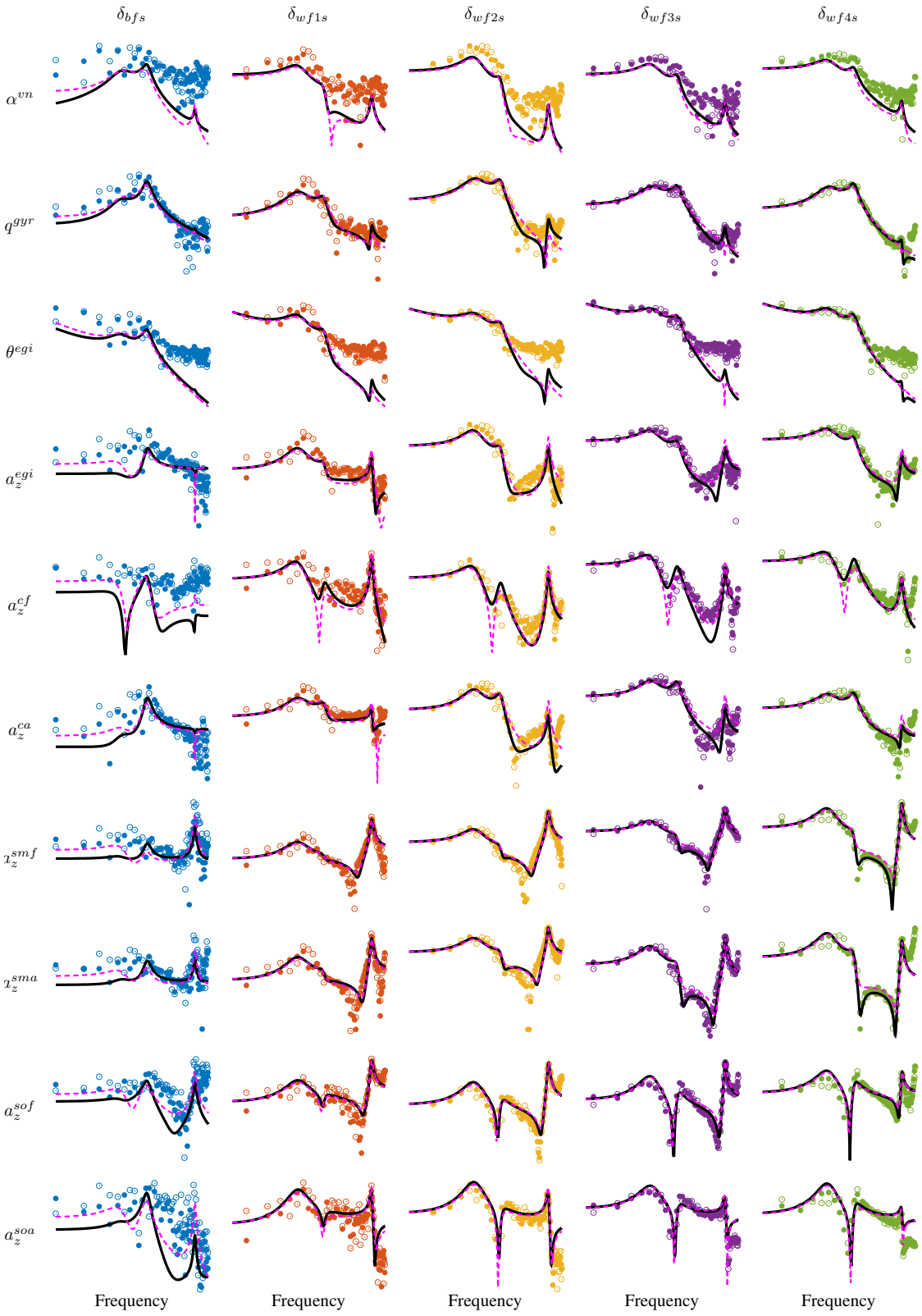

Fig. 18 Frequency response estimates as Bode magnitude plots for X-56A flight test data.

estimation, it is important to have input frequencies on distinct inputs, or for the case of feedback explored in this paper, account for those correlated secondary inputs.

The method is intended for frequency response estimation and is therefore restricted to small perturbation data that may be reasonably well approximation by a linear system or a first-order describing function. The method is procedural and does not require tuning parameters or engineering judgement. Although additional computations are needed to account for correlated secondary inputs, the method can be used with a recursive Fourier transform to run in real time during flight tests.

The main findings of this research may be summarized as the following:

1) The method accurately estimates frequency responses when input data contain correlated secondary inputs.
2) Estimated frequency response data agreed with results from parametric models identified using output error to match aircraft response data. Matching response data with output error is less sensitive to correlated input data.
3) Linear interpolation is an adequate approach for obtaining additional information to solve for the unknown frequency response evaluations. For the data examined here, only a slight degradation in accuracy was seen for a coarse frequency resolution.
4) The method can be used in real time during flight tests.

Acknowledgments

This research was supported by the NASA Advanced Air Transport Technology (AATT) Project. Gene Morelli at NASA Langley Research Center (LaRC) provided flight data for the T-2 aircraft, which was flown by the AirSTAR team under the NASA Aviation Safety Program, Vehicle Systems Safety Technologies (VSST) project. The efforts of the X-56A team at NASA Armstrong Flight Research Center (AFRC) are gratefully acknowledged. Numerical predictions of stability and control derivatives were supplied by Jeffrey Ouellette. Discussions with Chris Miller, Jeffrey Ouellette, Jacob Schaefer, and the other X-56A team members about the aircraft, flight test, and estimation results are appreciated.

References

[1] Morelli, E., and Klein, V., *Aircraft System Identification: Theory and Practice*, 2nd ed., Sunflyte, 2016.

[2] Klein, V., and Murphy, P., "Aerodynamic Parameters of High Performance Aircraft Estimated from Wind Tunnel and Flight Test Data," NATO RTO-MP-11, Madrid, Spain, 1998, pp. 18.1–18.20.

[3] Tischler, M., and Remple, R., *Aircraft and Rotorcraft System Identification: Engineering Methods with Flight Test Examples*, 2nd ed., Education series, AIAA, 2012.

[4] Knapp, M., Berger, T., Tischler, M., Cotting, M., and Marcus, A., "Development of a Full Flight Envelope F-16 VISTA Simulation MOdel from Closed-loop Flight Data," AIAA, Kissimmee, FL, 2018.

[5] Berger, T., Tischler, M., Knapp, M., and Lopez, M., "Identification of Multi-Input Systems in the Presence of Highly Correlated Inputs," *Journal of Guidance, Control, and Dynamics*, Vol. 41, No. 10, 2018, pp. 2247–2257.

[6] Grauer, J., and Morelli, E., "Method for Real-Time Frequency Response and Uncertainty Estimation," *Journal of Guidance, Control, and Dynamics*, Vol. 37, No. 1, 2014, pp. 336–343.

[7] Morelli, E., "System IDentification Programs for AirCraft (SIDPAC) version 4.1," NASA Software Catalog `http://software.nasa.gov`, September 2018.

[8] Morelli, E., "Multiple Input Design for Real-Time Parameter Estimation in the Frequency Domain," IFAC, Rotterdam, The Netherlands, 2003.

[9] Morelli, E., "Flight-Test Experiment Design for Characterizing Stability and Control of Hypersonic Vehicles," *Journal of Guidance, Control, and Dynamics*, Vol. 32, No. 3, 2009, pp. 949–959.

[10] Milliken, W., "Progress in Dynamic Stability and Control Research," *Journal of the Aeronautical Sciences*, Vol. 14, No. 9, 1947, pp. 493–519.

[11] Morelli, E., "High Accuracy Evaluation of the Finite Fourier Transform Using Sampled Data," Tech. Rep. TM-110340, NASA, Hampton, VA, June 1997.

[12] Morelli, E., and Grauer, J., "Practical Aspects of the Frequency Domain Approach for Aircraft System Identification," AIAA, Atlanta, GA, 2018.

[13] Morelli, E., "Flight Test Maneuvers for Efficient Aerodynamic Modeling," *Journal of Aircraft*, Vol. 49, No. 6, 2012, pp. 1857–1867.

[14] Maine, R., and Iliff, K., "Application of Parameter Estimation to Aircraft Stability and Control: the Output-Error Approach," Tech. Rep. RP-1168, NASA, Edwards, CA, June 1986.

[15] Grauer, J., "Dynamic Modeling using Output-Error Parameter Estimation based on Frequnecy Responses Estimated with Multisine Inputs," Tech. Rep. TM-2018-220108, NASA, Hampton, VA, November 2018.

[16] Morelli, E., "Dynamic Modeling from Flight Data with Unknown Time Skews," *Journal of Guidance, Control, and Dynamics*, Vol. 40, No. 8, 2017, pp. 2083–2091.

[17] Grauer, J., and Boucher, M., "Identification of Aeroelastic Models for the X-56A Longitudinal Dynamics Using Multisine Inputs and Output Error in the Frequency Domain," *MDPI Aerospace*, Vol. x, No. x, 2018, pp. x–x.